Journal of The Electrochemical Society, **161** (10) F1053-F1060 (2014)
0013-4651/2014/161(10)/F1053/8/$31.00 © The Electrochemical Society

A Complexed Sol-Gel (CSG) Approach to High Surface Area (HSA) Durable Ultra Active Platinum-Ruthenium Electro-Catalysts for Direct Methanol Fuel Cells

Karan Sandeep Kadakia,[a,*] Moni Kanchan Datta,[b,c] Oleg I. Velikokhatnyi,[b,c] Prashanth Jampani Hanumantha,[a,*] Sung Kyoo Park,[b] Sung Jae Chung,[d] Dae Ho Hong,[b] James A. Poston,[e] Ayyakkannu Manivanan,[e,] and Prashant N. Kumta[a,b,c,d,f,**,z]**

[a]*Chemical and Petroleum Engineering, Swanson School of Engineering, University of Pittsburgh, Pittsburgh, Pennsylvania 15261, USA*
[b]*Department of Bioengineering, Swanson School of Engineering, University of Pittsburgh, Pittsburgh, Pennsylvania 15261, USA*
[c]*Center for Complex Engineered Multifunctional Materials, University of Pittsburgh, Pennsylvania 15261, USA*
[d]*Mechanical Engineering and Materials Science, Swanson School of Engineering, University of Pittsburgh, Pittsburgh, Pennsylvania 15261, USA*
[e]*US Department of Energy, National Energy Technology Laboratory, Morgantown, West Virginia 26507, USA*
[f]*School of Dental Medicine, University of Pittsburgh, Pittsburgh, Pennsylvania 15217, USA*

Direct Methanol Fuel Cell (DMFC) is a promising power source for continuous generation of energy without evolution of any toxic by-products and greenhouse gases. Pt-Ru has been the accepted gold standard anode electro-catalyst for DMFC, but significant advances are required to enhance its performance and stability. A complexed sol-gel (CSG) approach has been used to develop nanostructured powder materials. Herein we report a novel CSG process to synthesize nanoparticulate high specific surface area (HSA), completely unsupported Pt(Ru) based electro-catalyst exhibiting three fold higher electrochemically active surface area (ECSA) and ultra high electrochemical performance compared to commercially available Johnson Matthey Pt-Ru black catalyst, the currently accepted gold standard. Furthermore, in identical single full cell DMFC configuration tests for methanol oxidation, current and power densities ∼40% higher than that displayed by Johnson Matthey catalyst is achieved.

Manuscript submitted March 24, 2014; revised manuscript received July 9, 2014. Published July 23, 2014. This was Paper 227 presented at the Seattle, Washington, Meeting of the Society, May 6–10, 2012.

Proton exchange membrane fuel cells (PEMFCs) are ubiquitously known for efficient continuous energy and power generation with reduced greenhouse emissions. Commercialization of low cost PEMFCs have however been thwarted by inferior catalyst activity and stability hence limited by loading constraints.[1–4] Of the different fuel cell types, PEMFCs, utilizing hydrogen as the fuel operating at low temperature (<120°C), has been considered for applications that require faster start-up times, and frequent starts and stops such as automotive applications, material handling equipment, and auxiliary backup power systems.[1–5]

On the other hand, methanol-powered direct methanol fuel cell (DMFC) are well suited for portable power applications in consumer electronic devices wherein the power requirements are low.[3–7] A significant fraction of the cost of DMFC and PEMFC arises from the use of precious metal catalysts hitherto platinum group-metal (PGM) catalysts currently used to accelerate electrochemical reactions at the electrodes.[3–8] For widespread commercialization of PEMFC and DMFCs, there is a critical need for continued advancements to minimize PGM loading or the development of equally performing non-PGM catalysts alternatives to reduce the cost.[3–10] The durability of catalysts is also a major issue under conditions of load-cycling in harsh corrosive environment. Mitigation of catalyst dissolution/degradation during operation of low and high-temperature fuel cells will certainly translate alone to higher performance leading to reduce costs.[3–11] Moreover, while addressing cost and durability, fuel cell performance and efficiency must also meet or exceed that of competing technologies (e.g. battery) to allow for market penetration and the benefits of this technology.

In light of the current situation, it is of paramount importance to design and synthesize effective electro-catalysts with improved electrochemical activity, improved durability/stability, and significantly reduced precious metal loading to ultra-low levels exhibiting enhanced tolerance to air, fuel and system-derived impurities. To meet these tremendous constraints on performance and efficiency, durability and cost requirements of fuel cells, significant research has been conducted over the years focusing largely on identifying new materials, and developing novel design and fabrication methods for catalysts and supports.[3–15] Despite myriad efforts, the platinum catalyst is extremely sensitive to CO poisoning, making it necessary to employ an additional reactor, which adds to the cost, to reduce CO in the fuel gas if the hydrogen is derived from an alcohol or hydrocarbon fuel for PEMFC.[3–13] Carbon monoxide generated during methanol oxidation reaction (MOR) as it is the surface bound intermediate at low temperatures during DMFC operation further inevitably leads to poisoning of the platinum catalyst surface which reduces the catalytic activity of platinum thus causing it to become inactive if used by itself.[3–7,12,16] It is widely accepted that platinum/ruthenium catalysts improve the CO tolerance of Pt catalysts.[3–18] It has also been reported that the electrocatalytic activity of a Pt-Ru catalyst with a Ru-decorated Pt surface in MOR is twice higher for optimized Ru coverage as compared to Johnson Matthey Pt-Ru black alloy [JM-Pt(Ru)] catalysts.[6,12,19] Contrary to the Ru-decorated Pt, the structure of Pt-decorated Ru is more attractive for improving mass activity due to the low Pt content in the catalysts[6,20,21] Kaplan et al.[21] showed that a Ru core-Pt shell catalyst performed much better (up to 36%) at high temperatures than a JM-Pt(Ru) alloy catalyst, but displayed only a moderate improvement in the chronoamperometry (stability) test. It has been reported that well alloyed Pt-Ru catalysts have lower rates of Ru dissolution and, therefore, exhibit better service life.[22,23] Previous studies[3–23] therefore clearly demonstrated that design and synthesis of robust electrocatalysts exhibiting high electrochemically active surface area (ESCA) with a suitable microstructure is expected to improve the electrocatalytic activity, reduce the cost by ultra-low PGM loading and further decrease the rate of dissolution of catalyst. Improvements in synthesis and design of the catalysts continues to be an area of intense research activity competitively pursued by researchers all over the world.

In this context, a novel complexed sol-gel process (CSG) has been developed by our group to synthesize unsupported nanocrystalline Pt-Ru based binary, ternary and quaternary solid solutions having high ESCA with excellent electrochemical activity and durable microstructure for the methanol oxidation reaction.[24–26] The present report

*Electrochemical Society Student Member.
**Electrochemical Society Active Member.
zE-mail: pkumta@pitt.edu

documents the recent results on improved activity of binary catalysts developed by the novel approach.

Experimental

Preparation of Electro-catalyst.— Phase-pure and high-surface-area Pt-Ru based catalysts were synthesized using the complexed sol-gel synthesis method. Platinum(II) acetylacetonate [Pt-acac: $Pt(C_5H_7O_2)_2$, Alfa Aesar], ruthenium(III) acetylacetonate [Ru-acac, $Ru(C_5H_7O_2)_3$, Alfa Aesar] were used as the sources for Pt and Ru respectively. Pt-acac and Ru-acac of the composition Pt-50 at.% Ru was dissolved at 50°C in100 ml of acetone. Tetramethylammonium hydroxide [TMAH, $(CH_3)_4NOH$, 25% in methanol, Alfa Aesar], set at TMAH : (Pt+Ru) = 1.75:1, was then added to the solution to serve as a hydrolyzing agent. Pt-acac and Ru-acac tend to phase separate during drying and evaporation of the solvent. Thus, the addition of tetramethylammonium hydroxide (TMAH), and its intended dual role to complex and induce hydrolysis of the starting noble metal precursors was found to be beneficial in yielding homogeneous amorphous gels containing Pt and Ru. The hydrolysis of platinum and ruthenium in this procedure occurs without phase separation as a result of the complexation of the precursors in the presence of TMAH. The TMAH results in complexation of the Pt-acac and Ru-acac precursors rather than precipitation of the hydroxides. The complexation reactions results in the formation of a gel rather than particulate which would have been the case should the reaction follow a typical hydroxide precipitation reaction as in the case of complete and rapid hydrolysis of alkoxide precursors in conventional sol-gel reactions. Thus unlike the alkoxide gels, acetyl-acetonate precursors result in a complexed intermediate which allows for a reduction procedure in which the two metal atoms form a uniform solid-solution. After stirring for some time, the solvent was evaporated until the solution became viscous, transforming into a thixotropic gel. The viscous gel was dried in air at 393 K for 12 hours. The dried powder was then heat treated in ultra-high purity (UHP) argon at 773 K in order to decompose the amorphous gel structure. The powders were then subsequently heat treated repeatedly in UHP Ar-1% O_2 gas at a lower temperature of 473 K than that reported earlier [24–26] based on the results of the thermo-gravimetric and differential thermal analysis (TGA-DTA). The heat treatments in UHP Ar-1% O_2 helped in removing the carbon in a controlled manner ensuring no oxidation of the alloy. The novelty of this procedure is that the heat treatments are conducted at a much lower temperature of 473 K, and this was performed repeatedly to achieve much reduced amounts of carbon as opposed to the two heat treatments in UHP Ar -1% O_2 at 573 K that was conducted in our previous published reports.[24–26]

Materials characterization.—X-ray diffraction, thermal and microstructural analysis.—In order to perform qualitative phase analysis, the Pt-Ru alloy were characterized by X-ray diffraction (XRD) using a Philips XPERT PRO system employing CuK_α ($\lambda = 0.15406$ nm) radiation with operating voltage and current at 45 kV and 40 mA, respectively. In order to understand the phase formation and decomposition temperature, thermogravimetric and differential thermal analysis (TGA-DTA) has been conducted on the as-prepared precursors as well as thermally treated powders using a TGA-DTA machine (Netzsch STA 09PC/4/H/Luxx TG-DTA). The TGA-DTA analysis has been carried out employing a heating rate of 10 K/min from room temperature up to 750 K in air. To investigate the microstructure of CSG-Pt(Ru), transmission electron microscopy (TEM) and high resolution transmission electron microscopy (HRTEM) was conducted. JEOL 4000EX operating at 400 kV was employed for conducting the TEM analysis to evaluate the particle size and the structure of particles. HRTEM analysis was conducted on the sample using JEOL JEM-2100F to investigate the particle size and morphology. Specific surface area of the catalyst was measured using the Brunauer-Emmett-Teller (BET) technique.

X-ray photoelectron spectroscopy (XPS).—X-ray photoelectron spectroscopy (XPS) was used to investigate the valence states of Pt and Ru ions. All the catalysts were analyzed by XPS using a Physical Electronics (PHI) model 32-096 X-ray source control and a 22-040 power supply interfaced to a model 04-548 X-ray source with an Omni Focus III spherical capacitance analyzer (SCA). The system is routinely operated within the pressure range of 10^{-8} to 10^{-9} Torr (1.3×10^{-6} to 1.3×10^{-7} Pa). The system was calibrated in accordance with the manufacturer's procedures utilizing the photoemission lines E_b of Cu $2p_{3/2}$ - 932.7 eV, E_b of Au $4f_{7/2}$ - 84 eV and E_b of Ag $3d_{5/2}$ - 368.3 for a magnesium anode. All the reported intensities are experimentally determined peak areas divided by the instrumental sensitivity factors. Charge correction was obtained by referencing the adventitious C 1s peak to 284.8 eV.

Membrane electrode assembly (MEA) preparation.— Catalyst ink was prepared for use in various characterization tests viz. cyclic voltammetry, chronoamperometry and single cell testing. The catalyst ink consisted of 85 wt% catalyst and 15 wt% Nafion 117 solution (5 wt% solution in lower aliphatic alcohols, Sigma-Aldrich). For the single cell testing, a membrane electrode assembly was fabricated by using a Nafion 115 membrane sandwiched between the two gas diffusion electrodes coated with the catalyst ink. Cathode used for the single cell test was Platinum black (Sigma Aldrich). The Nafion 115 membrane was pretreated first with a 3 wt% hydrogen peroxide solution to its boiling point in order to oxidize any organic impurities. Subsequently, it was boiled in D.I. water followed by immersion in a boiling 0.5 M sulfuric acid solution to eliminate any metallic impurities. Finally, it was treated multiple times in D.I water to remove any traces of remnant acid. This membrane was then stored in D.I. water to avoid dehydration. The membrane electrode assembly (MEA) was then fabricated by placing the two nafion impregnated electrodes (anode and cathode) on both sides of the wet pretreated nafion membrane. This assembly was then hot-pressed in a 25 T hydraulic lamination hot press with dual temperature controller (MTI Corporation) at a temperature of 125°C. The pressure applied was approximately 40 atm for ~30 seconds to ensure good contact between the electrodes and the membrane. This MEA is then used in the single cell test analysis.

Electrochemical Characterization.— Electrochemical characterization was conducted on the sample using a five port jacketed reaction cell (Ace Glass Inc.) to assemble a 3-electrode test system. The testing was done using a VersaSTAT 3 (Princeton Applied Research). A solution of 1 M methanol and 0.5 M sulfuric acid was used as the electrolyte which also served as the fuel. The solution is kept at a constant temperature of 40°C using a Fisher Scientific 910 Isotemp Refrigerator Circulator. The working electrodes were prepared by uniformly spreading the catalyst ink on teflonized carbon papers in an area of 1 cm^2. The JM-Pt(Ru) and the CSG-Pt(Ru) catalyst have been tested thorughout the article in identical conditions. All half-cell tests have been conducted by using the teflonized carbon paper as the current collector. The JM Pt-Ru catalysts and the CSG Pt-Ru catalysts have both been supported on the current collector (teflonized carbon paper) for all the tests reported herein. No other carbon support material has been added to either the JM or the CSG-derived Pt-Ru catalyst.The platinum loading on all the tested electrodes was maintained at ~0.2 mg/cm^2. The reference electrode was an XR 200 mercury/mercurous sulfate electrode [Hg/Hg_2SO_4] (Radiometer Analytical) that has a potential of ~ +0.654 V with respect to the Normal Hydrogen Electrode (NHE). Platinum foil (Alfa Aesar, 0.25 mm thick, 99.95%) was used as the counter electrode. Polarization was conducted at a scan rate of 10 mV/s from 0 V to 1 V vs. NHE. The solution was circulated past the electrode at ~200 rpm in the half-cell set up using a magnetic stir bar.

In order to obtain complete chemisorption of CO on the Pt sites, ultrahigh purity (UHP) nitrogen-1% CO mixture was passed in a solution of 0.5 M sulfuric acid for 30 minutes at 0.0 V with respect to normal hydrogen electrode (NHE). Nitrogen is then passed for 40 minutes to remove any CO traces from the electrolyte solution. CO stripping voltammetry was done in the same 3-electrode test system using a VersaSTAT 3 (Princeton Applied Research). The potential

was scanned back and forth twice from 0 to 1.2 V vs. NHE at a scan rate of 10 mV/s under UHP N_2 atmosphere. The working electrodes were prepared in the same manner as described previously by uniformly coating the catalyst ink to yield a catalyst loading of ~0.2 mg/cm^2. The temperature at which CO stripping was conducted was 25°C.

Chronoamperometry (current signal vs. time) was performed in a 3-electrode test system at a constant voltage of ~0.65 V vs. NHE. The same 3-electrode test system assembly as described above was used with the same electrodes and conditions. Elemental analysis of the media collected after the stability testing was performed by inductively coupled plasma optical emission spectroscopy (ICP-OES, iCAP 6500 duo Thermo Fisher) in order to determine the amount of platinum and ruthenium leached into the solution. The appropriate standards for obtaining the calibration lines were procured from Sigma Aldrich (platinum standard for ICP and ruthenium ICP/DCP standard solution). The solutions were then diluted with the stock solution that was used for electrochemical testing and chronoamperometry (i.e. 1 M methanol and 0.5 M sulfuric acid).

Single cell test analysis.— The three layer membrane electrode assembly (MEA) prepared was sandwiched between two Teflon gaskets with high precision thickness which are capable of withstanding the torque applied equally to the gaskets. This five layer assembly is then placed in between two fuel cell grade isotropic graphite blocks (ElectroChem Inc.) having a serpentine flow pattern and an active area of 1 cm^2. Two gold plated copper plates are then attached on the outer side which serve as the current collector plates. These plates have a silicone rubber heater which helps in providing the highest watt density and maintaining uniform cell temperature using the graphite blocks of high thermal conductivity. 1 M methanol is used as the fuel and UHP oxygen is used as the oxidant for the single cell test analysis. Current-voltage curves were measured galvanostatically by using an automatic electronic load generated by the fuel cell test set up obtained from Electrochem Incorporation at temperatures of 40°C, 60°C and 80°C, respectively.

Theoretical study.— Since Pt-Ru exists in fcc disordered configuration, we represented this solid solution as an intermetallic alloy with $L1_0$ tetragonal crystal structure and an approximate c/a ratio of ~ 1. Such an approximation is reasonable since we are interested in calculations of the relative energy differences between the various atomic configurations rather than the absolute values of the structures.

To model the Pt segregation, five layer slabs of (111) and (100) surfaces have been selected for the calculation of total energies for the different atomic distributions and Pt-compositions on the first two top layers one of which is an immediate subsurface layer and another representing the surface layer. Figure 1 shows a unit cell of the (111) slab containing two Pt and two Ru atoms on each layer. Segregation of Pt to the surface layer can be represented by exchange of corresponding Pt and Ru atoms between the two top layers. Since a periodic unit cell of the slab has been chosen in such a manner that each layer has two Pt and two Ru atoms, the first exchange of Pt and Ru atoms between the two top layers provides 75%Pt-25%Ru at the surface, while the second exchange of the atoms leads to the complete occupation of the surface layer by the Pt atoms and the subsurface layer by Ru atoms. The energy differential between an original non-segregated atomic distribution and these two partially segregated and fully segregated configurations gives the segregation energy of Pt to the surface. A negative value is an indication of the propensity to segregate, while a positive value would represent either Ru segregation or no segregation at all.

For the calculations, the five layer slab has been separated from its image perpendicular to the surface direction by a vacuum layer equal to the thickness of this five layer slab which is about 9 Å. In this study, the Vienna *Ab-initio* Simulation Package (VASP),[27–29] within the projector augmented-wave (PAW) method in the general gradient approximation (GGA)[30] for conducting the exchange-correlation

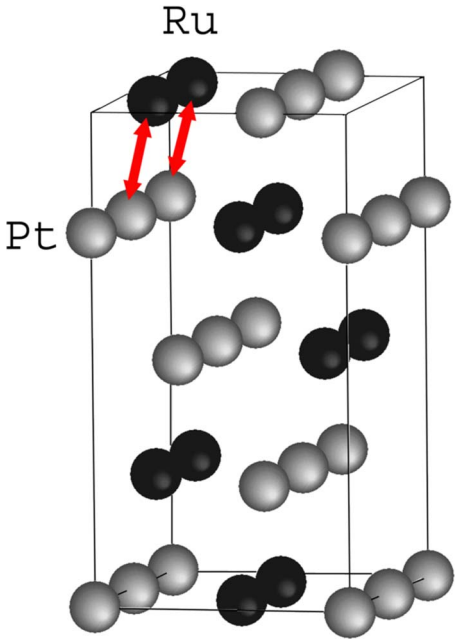

Figure 1. A unit cell of Pt-Ru (111) surface slab. Arrows denote Pt and Ru atoms exchanges modeling the surface segregation.

corrections has been used for calculation of the total energies, electronic structures and optimized lattice parameters of different atomic configurations and the corresponding crystallographic orientations of the Pt-Ru model system. Two bottom layers have been fixed with the interlayer distance corresponding to the calculated optimized bulk lattice parameters, while the top three layers were allowed to relax with the residual force components on each atom to be lower than ~0.01 eV/Å/atom, thus resulting in the accurate determination of the atomic positions and hence, the total energy of the whole system.

Results and Discussion

Nano-structure and surface area.— In this complexed sol-gel process, a homogeneous amorphous gel has been prepared by the complexation reaction between acetylacetonate complexes of the respective noble metals using tetramethyl ammonium hydroxide (TMAH) as the complexing agent.[24–26] The TGA-DTA analysis of the amorphous gel powder of Pt-Ru complex, performed in UHP-Ar atmosphere, shows that the decomposition of the gel powder is completed at about ~773 K as seen in Figure 2. The XRD analysis (Figure 3) of the heat treated powder obtained after thermal treatment of the gel powder at ~773 K for 4 hours in UHP-Ar atmosphere [denoted as CSG-Pt(Ru)/C] confirms the formation of nanocrystalline Pt-Ru solid solution. The high resolution TEM bright field image (HRTEM) along with SAD pattern of the thermally treated powder [CSG-Pt(Ru)/C], shown in Figure 4a, confirms the formation of nanocrystalline Pt(Ru) based alloy of particle size ~3–5 nm dispersed in the framework of the non-conducting amorphous carbon which will be hereafter denoted as CSG-Pt(Ru)/C. The non-conducting porous amorphous carbon, formed due to the decomposition of acetylacetonate complexes of Pt-Ru during pyrolysis, is expected to act as a nucleation site to nucleate nanocrystalline Pt(Ru) alloy on the surface of the carbon. The amorphous carbon also acts as a grain growth inhibitor for the Pt(Ru) alloy thus preventing significant grain growth at high temperature (~773 K). However, removal of the amorphous carbon is extremely important to obtain high surface area unsupported binary Pt(Ru) solid solution catalyst without inducing significant coarsening and oxidation of the catalyst. In the present work, an innovative thermal treatment process was implemented to remove the amorphous carbon which was further optimized to synthesize a phase-pure high CO tolerant Pt(Ru)

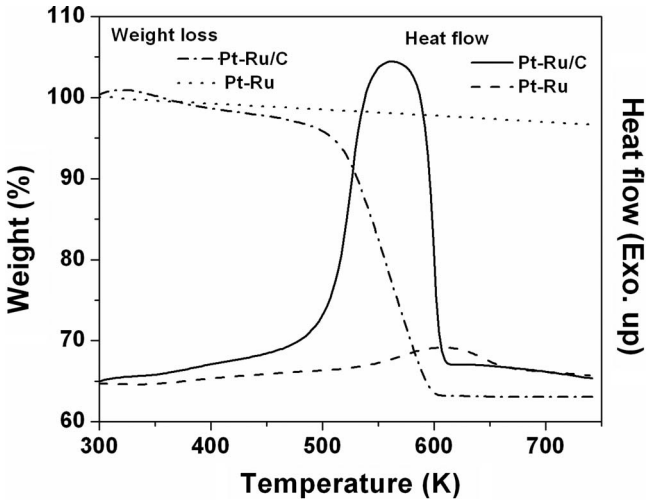

Figure 2. The TGA-DTA traces in air of CSG-Pt(Ru)/C show significant weight loss and confirming the exothermic oxidation of carbon. The CSG-Pt(Ru) catalyst shows negligible weight loss after multiple heat treatments in UHP Ar-1% O_2.

solid solution electro-catalysts, denoted as CSG-Pt(Ru). It should be noted that the synthesized CSG-Pt(Ru) alloy following the optimized controlled atmosphere heat-treatment which is effective in removing the carbon to form the high-surface-area catalyst, exhibits a very high electrochemically active surface area (ESCA) known to date to the best of our knowledge, displaying also ultra-high catalytic activity and durability.

The dried gel powder after heat-treatment in UHP-Ar at ~773 K for 4 hours yielded nanocrystalline alloy denoted as CSG-Pt(Ru)/C. However, the resultant composite alloy product contains a large amount of non-conducting amorphous carbon confirmed by the TGA-DTA analysis. The CSG-Pt(Ru)/C has a very low specific surface area of < 10 m^2/g due to the presence of the non-conducting carbon enveloping the metal alloy catalyst. The TGA-DTA trace in air as shown in Figure 1 shows an enormous weight loss from ~500 K - 573 K. This can be attributed to the oxidation and elimination of the carbon from CSG-Pt(Ru)/C. The low temperature oxidation of carbon might be due to some catalytic activity of the noble metals Pt and Ru in the powder. In order to remove this non-conducting carbon and generate phase-pure nanocrystalline Pt-Ru solid solution without oxidizing any

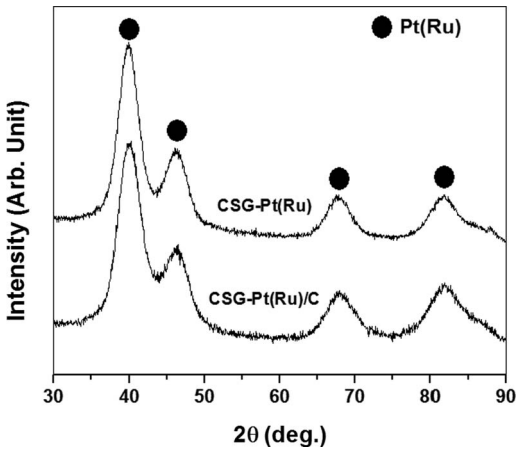

Figure 3. X-ray diffraction patterns of CSG-Pt(Ru)/C and CSG-Pt(Ru) obtained after thermal treatment of amorphous gel powder in UHP-Ar at ~773 K for 4 h and sequential multiple thermal treatments at ~473 K under UHP-Ar-1% O_2 atmosphere, respectively.

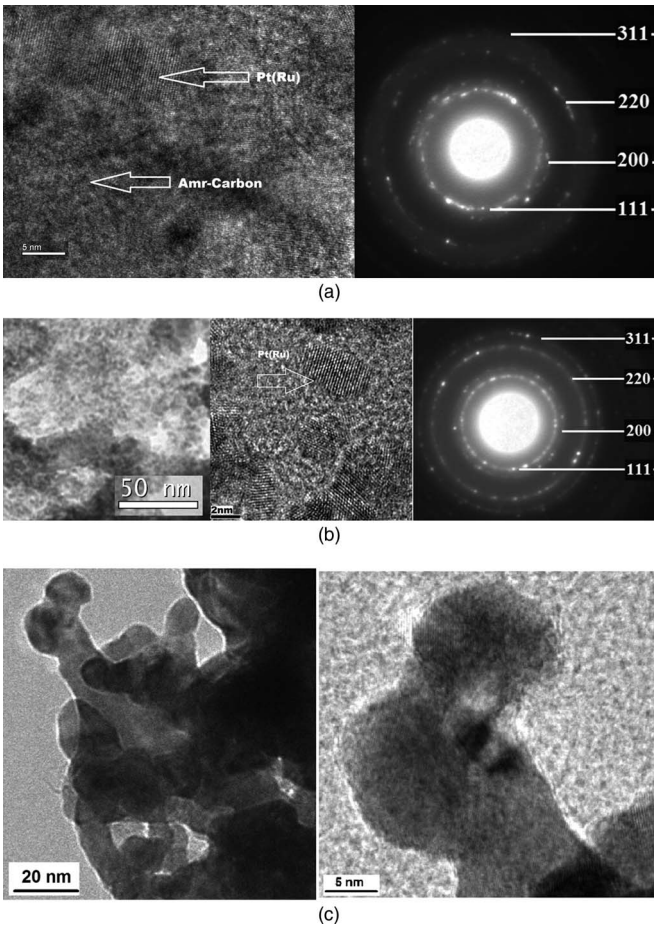

Figure 4. (a) HRTEM images along with SAD pattern of CSG-Pt(Ru)/C shows the formation of nanocrystalline Pt(Ru) alloy (~3–5 nm) dispersed in the framework of amorphous C. (b) TEM images along with SAD pattern of CSG-Pt(Ru) shows the formation of unsupported nanocrystalline Pt(Ru) alloy (~3–5 nm) and the corresponding HRTEM images shows lattice fringes of (111) plane of Pt(Ru) with a interplaner spacing 0.225±0.004 nm. (c) The HRTEM images of JM-Pt(Ru) showing a crystallite size of ~10 nm.

of the noble metals, multiple heat treatments in UHP Ar-1% O_2 gas at ~473 K were performed. The 1% O_2 present in the gas facilitated the controlled removal of carbon without oxidizing the noble metals, finally yielding a single phase nanocrystalline Pt(Ru) alloy. A lower temperature of ~473 K was selected because the TGA-DTA trace showed that the oxidation of carbon commenced at ~500 K (Figure 1). Since the TGA-DTA analysis is a dynamic process, we hypothesized that carbon removal is initiated at a lower temperature. Also, a lower heat-treatment temperature in the presence of 1% O_2 would ensure minimum or no significant oxidation of the resulting alloy. After the final heat-treatment, we indeed observed marginal weight loss in the TGA-DTA analysis which may be attributed to minimal (~3 wt%) carbon and/or moisture present in the sample. DTA trace also does not show any significant exothermic reaction confirming the removal of carbon. The C and/or moisture present in the sample would not show more weight loss in the TGA-DTA at higher temperatures (over ~673 K)

The XRD patterns of the CSG-Pt(Ru) catalyst, after multiple heat treatments at ~473 K in UHP Ar-1% O_2, seen in Figure 3, shows the presence of only fcc-Pt(Ru) peaks without any detectable phase separated hcp-Ru or RuO_2 peaks corresponding to any crystallized phases following the controlled UHP Ar-1% O_2 treatments to remove the amorphous carbon derived from the carbonization of the gel. The calculated (111) inter-planer spacing (d_{111}) of fcc-Pt(Ru) is ~0.223 nm which clearly suggests the formation of solid solution of Ru in

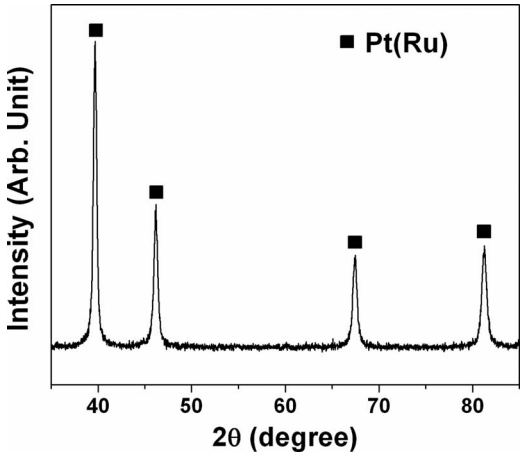

Figure 5. X-ray diffraction pattern of the CSG-Pt(Ru) electro-catalyst after heat-treatment in UHP-Ar at ∼873 K confirming presence of only fcc-Pt(Ru) phase.

Pt.[31,32] However, the formation of any amorphous noble metal oxide cannot be discounted. In order to completely confirm the formation of the single phase Pt(Ru) alloy with no presence of any noble metal oxide, the CSG-Pt(Ru) electro-catalyst derived from the UHP Ar-1% O_2 heat-treatment was further subjected to heat-treatment in UHP-Ar atmosphere alone to higher temperatures of ∼873 K in order to determine the presence of any phase separated Ru or any crystallized RuO_2 present in the CSG-Pt(Ru) catalyst. At this temperature and treatment any amorphous phase present should undergo crystallization forming the crystalline oxide phase. The XRD pattern shown in Figure 5 indicates only crystalline fcc Pt(Ru) peaks with no additional peak of hcp-Ru or RuO_2, confirming the formation of only single phase solid solution of Pt-Ru in the CSG-Pt(Ru) catalyst clearly obviating the presence of any phase separation and formation of any oxide phase. The narrow crystalline peaks observed (Figure 5) are due to the expected diffusion induced grain growth owing to the heat-treatment of the fully synthesized electro-catalyst [CSG-Pt(Ru)] in UHP-Ar at higher temperatures of ∼873 K. The absence of any crystaline noble metal oxide peaks in the UHP-Ar heat treated catalyst obtained after the controlled heat treatments to eliminate carbon is an indication that there is very minimal or no oxide phase present in the synthesized electro-catalyst obtained after the controlled heat-treatment.

The TEM bright field image along with selected area diffraction (SAD) pattern of CSG-Pt(Ru), shown in Figure 4b, confirms the formation of nanosized Pt(Ru) particles with a crystallite size of ∼3–5 nm which is similar to CSG-Pt(Ru)/C (Figure 4a) suggesting no significant grain growth of Pt(Ru) during the carbon removal processes. The high resolution TEM image of CSG-Pt(Ru), seen in Figure 4b shows lattice fringes with a spacing of ∼0.225 ± 0.004 nm which corresponds to the (111) inter-planer spacing of face centered cubic Pt(Ru). The spacing observed between the lattice fringes of (111) plane of Pt(Ru) in the HRTEM image is in good agreement with the calculated d_{111} value (∼0.223 nm) from the XRD patterns further validating the formation of single phase fcc Pt(Ru) alloy with minimal or no oxide phases. In contrast, the crystallite size of the commercial JM catalyst lies in the range of ∼10 nm which was determined by TEM imaging shown in Figure 4c.

Theoretical calculatons and XPS studies.— Theoretical calculation gives the corresponding (111) inter-planar spacing (d_{111}) of disordered fcc-PtRu of 0.2247 nm, which is in excellent agreement with above mentioned experimental data. Usually, DFT calculations within the GGA approximation feature lower accuracy for calculated lattice parameters, however in the present case we deal with a bulk idealized fully ordered Pt-Ru structure ($L1_0$) instead of the disordered fcc nano-particles observed experimentally. Most likely, there is a cancellation of two errors in the calculations which arise from the choice of the ordered structure on the one hand, and approximation of the nano-particles by consideration of the simple bulk system on the other hand.

In addition to the different segregation energies, (111) and (100) surface energies for pure Pt, Ru and Pt-Ru alloy within fcc and $L1_0$ configurations were also calculated. The results are summarized in Table I. One can see, that movement of the first Pt atom from the subsurface layer to the surface gives an energy difference of −0.95 eV, while the same action for Ru atom results in a positive change of the total energy equal to +0.87 eV. The second exchange between the corresponding Pt and Ru atoms lead to similar results of −0.70 and +0.55 eV for Pt and Ru segregation energies, respectively. Negative values for Pt and positive values of segregation energies for Ru point out to the fact that Pt demonstrates a strong propensity for segregation to the surface which is observed experimentally. Similar results have been obtained for Pt segregation to (100) surface wherein the energies also demonstrate negative values. One can therefore observe that Pt and Ru surfaces demonstrate the lowest and the highest energy values respectively with Pt-Ru surface energy in between, which additionally justifies the Pt segregation. This trend is also observed for (100) crystallographic orientation, which is expected. Thus, our theoretical consideration of Pt segregation indeed has demonstrated the propensity of Pt to segregate to the surface.

In order to determine the surface composition and chemical oxidation states of platinum and ruthenium, X-ray photoelectron spectroscopy (XPS) technique has been carried out for both CSG-Pt(Ru) and commercially obtained JM-Pt(Ru). The Pt 4f doublet peaks for the CSG-Pt(Ru), observed at ∼71.8 eV and ∼75.1 eV (Figure 6a), correspond to Pt $4f_{7/2}$ and Pt $4f_{5/2}$ binding energy, respectively, in the preferred oxidation state of zero. The shift of Pt $4f_{7/2}$ and Pt $4f_{5/2}$ of CSG-Pt(Ru) catalyst to slightly higher binding energy states in comparison to JM-Pt(Ru) catalyst might be due to the better alloying effect of Ru with Pt, which is expected to help in weakening the adsorption of CO [33,34] and as a result lead to a better electrochemical active catalyst as is shown by the results herein. A shift in the binding energy might also be because of the final state relaxation due to the nanoparticulate size effect and Pt-Ru interaction as reported in other publications.[35,36] In case of ruthenium, the Ru $3d_{3/2}$ spectrum overlaps the C1s spectrum which prevents the accurate determination of the oxidation states of ruthenium. However, the peak of Ru $3p_{3/2}$ spectrum, shown in Figure 6b, is observed at 462.5 eV and 462 eV for CSG-Pt(Ru) and the JM-Pt(Ru) catalyst, respectively. The surface

Table I. Segregation energies of Pt and Ru to (111) surface and Pt only to (100) surface for two corresponding Pt and Ru atoms exchange steps. Surface energies for pure Pt, Ru, and Pt-Ru are also presented for (111) and (100) crystallographic orientations.

Surface		(111) Pt / Ru		(100) Pt	
	E_{segr}	50–75	75–100	50–75	75–100
	(eV/at)	−0.95 /+0.87	−0.70 / +0.55	−1.22	−0.97
	E_{segr} (eV/at) average	−0.82/+0.71		−1.08	
E_{surf} (J/m^2)	Pt-Ru	1.88		2.15	
	Pt^{fcc}	1.54		1.83	
	Ru^{fcc}	1.95		2.24	

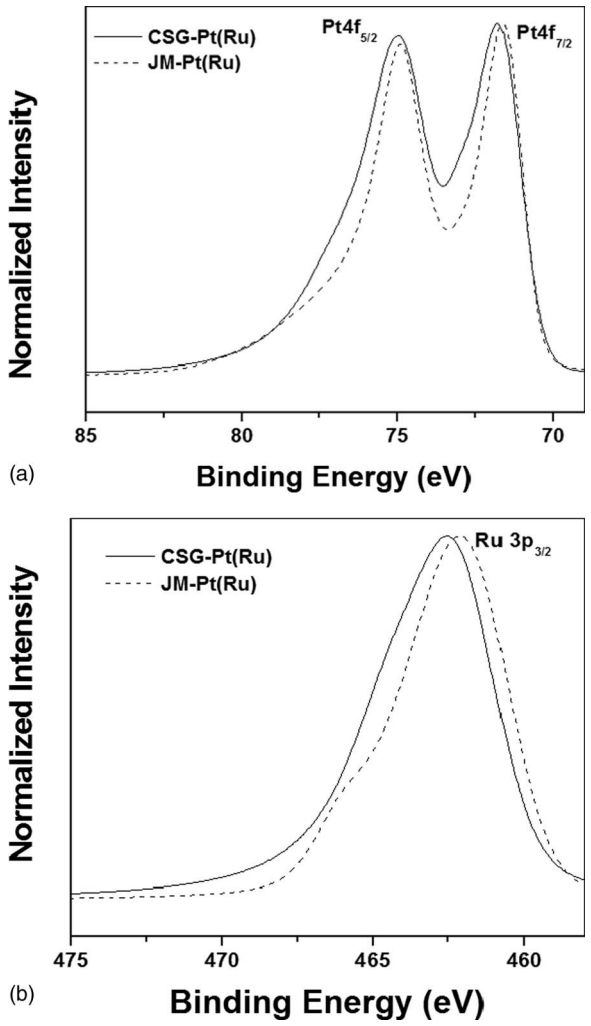

Figure 6. The XPS spectra of (a) Pt $4f_{7/2}$ and Pt $4f_{5/2}$ doublet, and (b) Ru $3p_{3/2}$ of CSG-Pt(Ru) and JM-Pt(Ru).

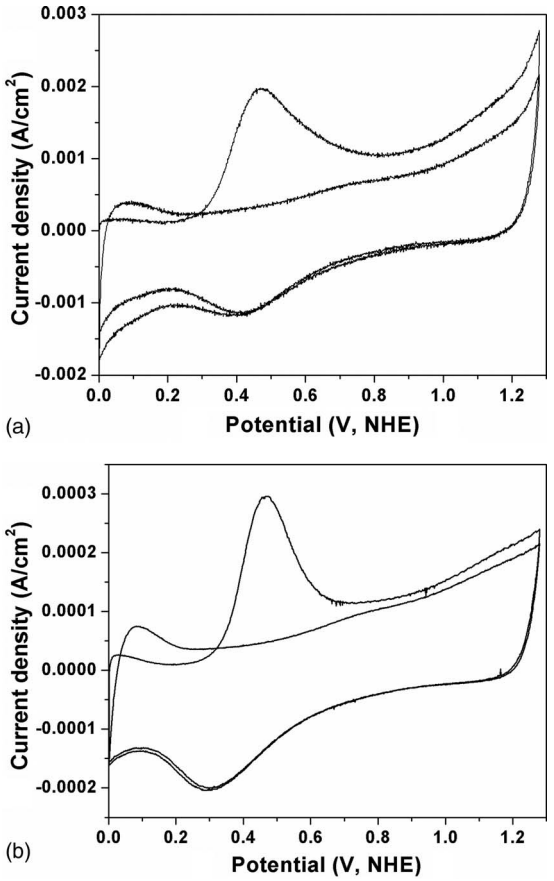

Figure 7. The CO stripping voltammetry curves of (a) CSG-Pt(Ru) and (b) JM-Pt(Ru) in 0.5M H_2SO_4 with a Pt loading of 0.2 mg/cm^2.

ratio of Pt/Ru, determined by the XPS, is 1.57 for the CSG-Pt(Ru) corresponding to the composition of Pt-39at.% Ru and 1.44 for the JM-Pt(Ru) corresponding to the composition of Pt-41at.% Ru which indicates much higher Pt segregation on the surface and that the surface composition of CSG prepared Pt(Ru) is quite similar in comparison to JM-Pt(Ru) catalyst. It should also be noted that the electrochemically active Pt enrichment observed on the surface of the nanocrystalline Pt(Ru) catalyst determined by XPS is expected due to the lower cohesive energy of Pt (5.84 eV/atom) than Ru (6.74 eV/atom) determined from our theoretical studies described below.

An additional argument toward understanding of the Pt segregation might be obtained from the surface energy calculations for pure Pt, Ru and Pt-Ru alloy within fcc and $L1_0$ crystal structures with the cubic lattice parameter corresponding to the bulk Pt-Ru system and collected in Table I. The theoretical study based on Density Functional Theory (DFT), described in the methods section, also indicates the propensity of Pt for segregation to the surface of Pt-Ru alloy. The energy difference between an original non-segregated atomic distribution and segregated configurations gives negative segregation energy for Pt and positive values of segregation energies for Ru collected in Table I. The negative values for Pt segregation energy point out at the fact that Pt demonstrates a propensity for segregation to the surface which is observed experimentally and correlates well with other previously reported theoretical studies.[27–29] Similar results have been obtained for Pt segregation to both (111) and (100) surfaces although to different extents. An additional argument toward understanding of the Pt segregation might be obtained from the surface energy calculations for pure Pt, Ru and Pt-Ru alloy within fcc and $L1_0$ crystal structures with the cubic lattice parameter corresponding to the bulk Pt-Ru system and also collected in Table I. One can observe that Pt and Ru surfaces demonstrate the lowest and the highest energy values respectively with Pt-Ru surface energy in between, which additionally justifies the Pt segregation. This trend is also observed for (100) crystallographic orientation, which is expected. Thus, our theoretical study of segregation demonstrates the propensity of Pt to segregate to the surface which is in agreement with our experiments.

Electrochemical Tests.— The specific surface area, measured by the BET technique, of the CSG-Pt(Ru) catalyst is ~216.6 m^2/g which is three times higher than the commercially available JM-Pt(Ru) catalyst of specific surface area ~75 m^2/g. In order to determine the electrochemically active surface area (ECSA), which has greater influence on the electrochemical activity of the Pt(Ru) electro-catalyst, CO stripping voltammetry has been performed on both the CSG-Pt(Ru) and JM-Pt(Ru) catalyst. The CO stripping voltammetry curves of the CSG-Pt(Ru) catalyst and the commercially obtained JM-Pt(Ru) catalyst, shown in Figures 7a and 7b, respectively, shows the anodic peak potential for the CO oxidation to CO_2 occurring at ~0.47 V. A subsequent cyclic voltammogram, performed immediately after CO stripping, shown in Figure 7, confirms complete CO removal and the recovery of the activity of the catalyst. The difference in the areas of voltammogram between the two subsequent sweeps was calculated to determine the CO stripping charge. The charge obtained, after accounting for the scan rate of 10 mV/sec used for CO stripping, from the difference in areas between the curves for CSG-Pt(Ru) and JM-Pt(Ru) is ~0.0235 C and ~0.0753 C, respectively. The ECSA of the CSG-Pt(Ru) and JM-Pt(Ru) has been calculated assuming a

monolayer of adsorbed CO to be present on the catalyst surface corresponding to a charge density of 0.42 mC/cm^2 and normalized with respect to the Pt loading. It was found that the JM-Pt(Ru) catalyst exhibits an ECSA of ∼28.0 m^2/g whereas the CSG -Pt(Ru) catalyst exhibits an ECSA of ∼89.6 m^2/g which is correspondingly three fold higher than JM-Pt(Ru) catalyst similar to the difference in the BET surface area between the two systems. This clearly indicates that our nanocrystalline Pt(Ru) electro-catalyst prepared by the novel CSG method has more electrochemically active catalytic sites available for selective electrochemical reaction than the commercial JM-Pt(Ru) catalyst, though both exhibit similar surface and bulk composition.

Nanocrystalline Pt(Ru) alloy synthesized by the CSG process, exhibits high BET and ECSA surface areas, leading to a larger number of Pt active sites available on the surface of the alloy, and as a result excellent electrochemical activity is expected to be achieved. The electrochemical performance including activity and durability of CSG-Pt(Ru) electro-catalyst has been studied using the methanol oxidation reaction in a full cell assembly. In order to measure the electrochemical activity of the CSG-Pt(Ru) and JM-Pt(Ru) catalyst for MOR, the polarization test has been performed in the presence of 1 M methanol and 0.5 M sulfuric acid solution serving as a fuel after pre-conditioning the catalyst (with a Pt catalyst loading of ∼0.2 mg/cm^2). The polarization curve, obtained at a scan rate of 10 mV/sec at 40°C, shown in Figure 8a, indicates that the CSG-Pt(Ru) catalyst exhibits a current density of ∼40 mA/cm^2 at ∼0.65 V vs. NHE whereas the JM-Pt(Ru) catalyst shows a current density of ∼27 mA/cm^2 at the same voltage. It should also be noted that in our previous articles,[25,26] a current of ∼40 mA/1.5 cm^2 i.e. ∼26.6 mA/cm^2 was obtained at the same voltage. The current result also indicates ∼50% increase in the catalytic activity of the nanocrystalline Pt(Ru) electro-catalysts synthesized by the optimized CSG process reported herein. The result also indicates that the CSG-Pt(Ru) catalyst which has the same bulk and surface composition as commercially available JM-Pt(Ru) catalyst shows an increase of ca. 45% in the catalytic performance for methanol oxidation. The improved catalytic performance of CSG-Pt(Ru) is expected to arise due to the higher BET and ECSA surface areas, generated by the novel CSG process, in comparison to JM-Pt(Ru) catalyst.

Figure 8b compares the DMFC single cell test performance curves for the CSG-Pt(Ru) catalyst and the JM-Pt(Ru) catalyst with the catalyst loading normalized to ∼1 mg/cm^2 of Pt on the anode side and ∼2 mg/cm^2 of Pt black (Alfa Aesar) loading on the cathode side. The DMFC single cell performance, shown in Figure 8b, shows that the CSG-Pt(Ru) has better catalytic performance than the JM-Pt(Ru) catalyst at temperatures of ∼40°C, 60°C and 80°C, respectively. At a voltage of 0.2 V, the CSG-Pt(Ru) catalyst shows a current density of ∼140 mA/cm^2 at an operating temperature ∼80°C which is ∼40% higher than the JM-Pt(Ru) which exhibits a current density of ∼100 mA/cm^2. At the corresponding current densities, the CSG-Pt(Ru) catalyst also exhibits ∼40% higher power density (∼28 mW/cm^2) in comparison to JM-Pt(Ru) catalyst (∼20 mW/cm^2) at operating temperature 80°C (Figure 8c). The maximum power density obtained by the CSG-Pt(Ru) and JM-Pt(Ru) at each temperature is tabulated in Table II along with the corresponding voltage and current densities.

In order to study the durability/stability of the CSG-Pt(Ru) and JM-Pt(Ru) catalyst during MOR reaction, chronoamperometry (current vs. time) at a constant voltage of ∼0.65 V vs. NHE at 40°C in 0.5 M H_2SO_4 and 1 M CH_3OH solution has been performed to measure the degradation or loss of activity of the catalyst as a function of time. The chronoamperometry response, shown in Figure 9, over a period of 2 hours shows that the CSG-Pt(Ru) retains ∼87% of current density (∼40 mA/cm^2 to ∼35 mA/cm^2) whereas the commercial JM-Pt(Ru) retains only ∼66% of current density (∼27 mA/cm^2 to ∼18 mA/cm^2). In order to quantify the amount of platinum and ruthenium leached into the electrochemical electrolyte solution, the electrochemical solution after the testing time of 2 hours was collected and analyzed by inductively coupled plasma optical emission spectroscopy (ICP). It was determined that no active Pt leached into the solution for both the catalysts. However, ruthenium found in the

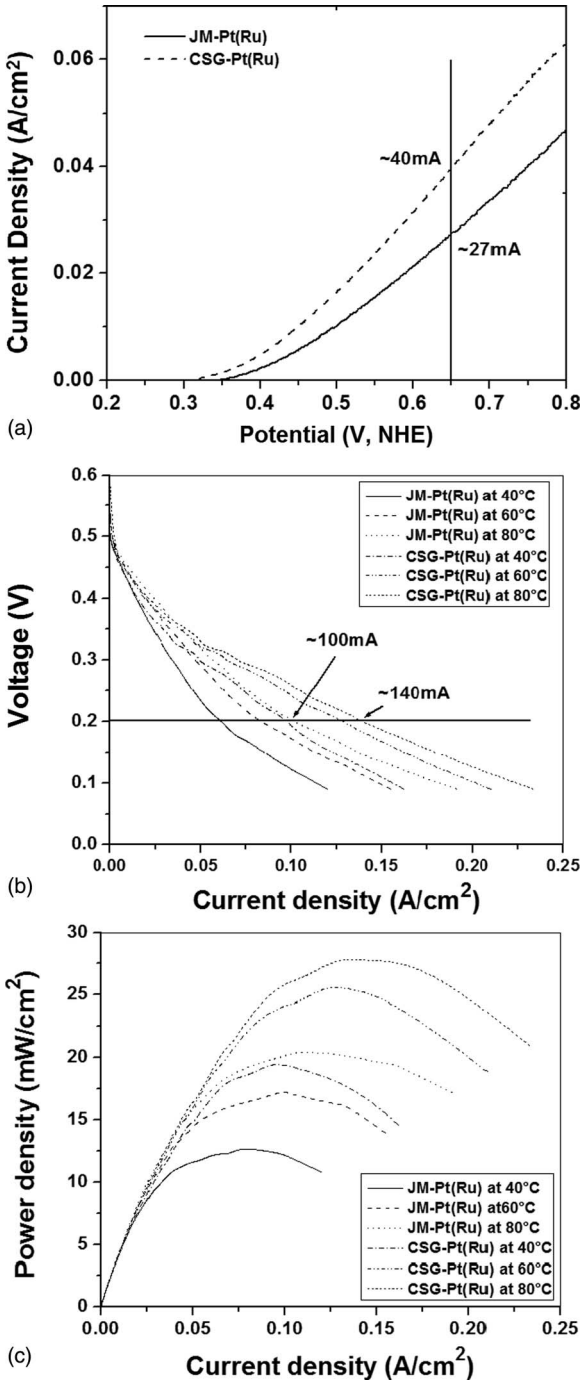

Figure 8. (a) The polarization curve CSG-Pt(Ru) and JM-Pt(Ru) tested at 40°C at a scan rate of 10 mV/sec and Pt loading of 0.2 mg/cm^2. (b) Polarization curve and (c) Power density performance of DMFC single cell testing at various temperatures of the CSG-Pt(Ru) and JM-Pt(Ru) anode.

solution for the CSG-Pt(Ru) and JM-Pt(Ru), was ∼0.064 ppm and ∼0.084 ppm, respectively indicating the superior durability of the CSG derived catalyst. The reduced amounts of Ru detected in the solution for the CSG-Pt(Ru) is possibly a reflection of the larger Pt surface segregation compared to the JM-Pt(Ru) catalyst minimizing the dissolution of Ru thus rendering the catalyst more stable. The fact that the CSG-Pt(Ru) electro-catalyst developed in the current work has much reduced amount of Ru leached out corroborates with the fact that the CSG-Pt(Ru) catalyst is much more robust and durable compared to that of the commercial JM-Pt(Ru) catalyst. The CSG-Pt-Ru exhibits slightly lower amount of ruthenium leached out in the

Table II. The maximum power density obtained for CSG-Pt(Ru) and JM-Pt(Ru) at each temperature along with the corresponding voltage and current densities.

Temperature →		40°C	60°C	80°C
Maximum power density (mW/cm^2)	JM-Pt(Ru)	13	17.5	20
	CSG – Pt(Ru)	19	26	28
Current density (mA/cm^2)	JM-Pt(Ru)	78	95	108
	CSG – Pt(Ru)	100	132	140
Corresponding voltage (V)	JM-Pt(Ru)	0.15	0.18	0.2
	CSG – Pt(Ru)	0.2	0.2	0.2

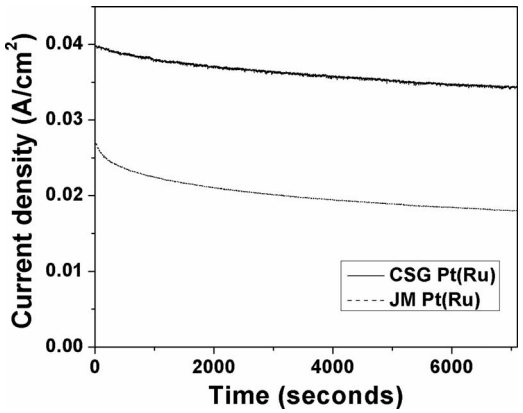

Figure 9. Chronoamperometry plot of CSG-Pt(Ru) and JM-Pt(Ru) for 2 h measured at 0.65 V vs. NHE in a mixture of 0.5 M H_2SO_4 and 1 M methanol at 40°C.

leachate compared to the JM-Pt-Ru material. We suspect that this could be a result of the slight differences in the surface composition as evidenced by the XPS data showing that the surface ratio of Pt/Ru is 1.57 for the CSG-Pt(Ru) (corresponding to the composition of Pt-39 at.% Ru) and 1.44 for the JM-Pt(Ru) (corresponding to the composition of Pt-41 at.% Ru). We thus suspect this to be the reason for the difference in the observed amounts of ruthenium in the leachate and thus the corresponding improvement in durability.

Conclusions

The present study demonstrates the successful synthesis of high ESCA Pt(Ru) based electro-catalyst generated by a novel CSG process with an innovative controlled heat-treatment protocol to generate also a very high-specific-surface-area (HSA) catalyst (~216.6 m^2/g) determined by BET with no phase separated metal or oxide phases. The CSG-Pt(Ru) alloy thus exhibits excellent electro-catalytic activity and higher durability reported to date, to the best of our knowledge with the ability to reduce the noble metal oxide loading to ultra-low levels with improved electro-catalytic performance and electrochemical stability.

Acknowledgments

Research supported in part by the National Science Foundation under award – CBET 0933141. Authors also acknowledge Pittsburgh Supercomputing Center for allocation of computational resources. PNK acknowledges the Edward R. Weidlein Chair Professorship funds and the Center for Complex Engineered Multifunctional Materials (CCEMM) for procuring the electrochemical equipment used in this research work.

P.N.K., M.K.D., O.I.V. and K.S.K. devised the original concept, designed the experiments and planned the theoretical studies. K.S.K., M.K.D., P.H.J. and S.K.P. synthesized the materials, prepared the electrodes and MEA, and performed the physio-chemical and electrochemical characterization. O.I.V. conducted the theoretical analyses. S.J.C. and D.H.H performed the TEM and HRTEM analyzes. J.A.P. and A.M. collected and analyzed the XPS data. K.S.K., M.K.D., O.I.V. and P.N.K. analyzed the data and wrote the first draft of the paper; and all authors participated in the manuscript revision. The project is conceived and supervised by P.N.K.

References

1. 2011 fuel cell technologies market report, U. S. Department of Energy, Energy efficiency and renewable energy (June 2011).
2. Fuel Cell Industry Analysis, RNCOS report (July 2012).
3. The department of energy hydrogen and fuel cell program plan, U.S. department of energy (November 2013).
4. 2013 Annual Merit Review Proceedings, Hydrogen and Fuel cell Program, U. S. Department of Energy (May 2013).
5. D. P. Wilkinson, J. Zhang, R. Hui, J. Fergus, and X. Li, *Proton exchange membrane fuel cell, Materials Properties and Performance*, ed., CRC Press, Boca Raton, FL (2010).
6. X. Zhao, M. Yin, M. Liang, L. Liang, C. Liu, J. Liao, T. Lu, and W. Xing, *Energy Enviorn. Sci.*, **4**, 2736 (2011).
7. H. Liu and J. Zhang, *Electrocatalysis of direct methanol fuel cell: From fundamentals to applications*, ed., Wiley-VCH Verlag GmbH & Co. KGaA, Weinheim (2009).
8. C. Wang, M. Waje, X. Wang, J. M. Tang, R. C. Haddon, and Y. Yan, *Nanolett.*, **4**, 345 (2004).
9. Basic Research Needs: Catalysis for energy, Report from the U. S. department of energy, Basic Energy science workshop (August 2007).
10. E. Proietti, F. Jaouen, M. Lefevre, N. Larouche, J. Tian, J. Herranz, and J. P. Dodelet, *Nature communications*, **2**, 416 (2011).
11. C. Zhou, F. Peng, H. Wang, H. Yu, C. Pang, and J. Yang, *Electrochemistry Communications*, **12**, 1210 (2010).
12. S. Alayoglu, A. U. Nilekar, M. Mavrikakis, and B. Eichhorn, *Nature Materials*, **7**, 333 (2008).
13. V. R. Stamenkovic, B. S. Mun, M. Arenz, K. J. J. Mayrhofer, C. A. Lucas, G. Wang, P. N. Ross, and N. M. Markovic, *Nature Materials*, **6**, 241 (2007).
14. A. V. Palenzuela, F. Centellas, J. A. Garrido, C. Arias, R. M. Rodriguez, E. Brillas, and P. L. Cabot, *J. Phys. Chem. C.*, **114**, 4399 (2010).
15. A. C. Garcia, V. A. Paganin, and E. A. Ticianelli, *Electrochimica Acta*, **53**, 4309 (2008).
16. A. Murty and A. Manthiram, *Electrochemistry Communications*, **13**, 310 (2011).
17. Z. G. Shao, F. Zhu, W. F. Lin, P. A. Christensen, and H. Zhang, *J. Power Sources*, **161**, 813 (2006).
18. T. Maiyalagan, T. O. Alaje, and K. Scott, *J. Phys. Chem. C.*, **116**, 2630 (2012).
19. F. Maillard, G. Q. Lu, A. Wieckowski, and U. Stimming, *J. Phys. Chem. B.*, **109**, 16230 (2005).
20. A. S. Arico, V. Baglio, A. D. Blasi, E. Modica, G. Monforte, and V. Antonucci, *J. Electroanalytical chemistry*, **576**, 161 (2005).
21. D. Kaplan, M. Alon, L. Burstein, Y. Rosenberg, and E. Pelad, *J. Power Sources*, **196**, 1078 (2011).
22. A. S. Arico, V. Baglio, E. Modica, A. Di Blasi, and V. Antonucci, *Electrochemistry Communications*, **6**, 164 (2004).
23. X. Cheng, C. Peng, M. You, L. Liu, Y. Zhang, and Q. Fan, *Electrochimica Acta*, **51**, 4620 (2006).
24. J. Y. Kim, Z. G. Yang, C. C. Chang, T. I. Valdez, S. R. Narayanan, and P. N. Kumta, *Journal of the Electrochemical Society*, **150**, A1421 (2003).
25. Y. M. Alyousef, M. K. Datta, S. C. Yao, and P. N. Kumta, *Journal of Physics and Chemistry of Solids*, **70**, 1019 (2009).
26. Y. M. Alyousef, M. K. Datta, K. Kadakia, S. C. Yao, and P. N. Kumta, *Journal of Alloys and Compounds*, **506**, 698 (2010).
27. G. Kresse and J. Furthmüller, *Physical Review B*, **54**, 11169 (1996).
28. G. Kresse and J. Furthmüller, *Computational Materials Science*, **6**, 15 (1996).
29. G. Kresse and D. Joubert, *Physical Review B*, **59**, 1758 (1999).
30. J. P. Perdew and W. Yue, *Physical Review B*, **33**, 8800 (1986).
31. G. F. Cabeza, P. Legare, and N. J. Castellani, *Surface Science*, **465**, 286 (2000).
32. S. Chen and K. Kimura, *Journal of Physical Chemistry B*, **105**, 5397 (2011).
33. M. R. Kim, S. J. Kim, and D. Jang, *Crystal Growth and Design*, **10**, 257 (2010).
34. M. Wakisaka, S. Mitsui, Y. Hirose, K. Kawashima, H. Uchida, and M. Watanabe, *Journal of Physical Chemistry B*, **110**, 23489 (2006).
35. Y. T. Kim and T. Mitani, *J. Catal.*, **238**, 394 (2006).
36. R. Ahmadi, M. K. Amini, and J. C. Bennett, *J. Catal.*, **292**, 81 (2012).